Garnet-Type Lithium Ion Conducting Oxides: $Li_7La_3Zr_2O_{12}$ and Its Chemical Derivatives

Junji Akimoto, Naoki Hamao, and Kunimitsu Kataoka

Abstract Recent advancements of garnet-type lithium ion conducting oxide materials such as $Li_7La_3Zr_2O_{12}$ and its chemical derivative $Li_{6.5}La_3Zr_{1.5}Ta_{0.5}O_{12}$ are reviewed. A relationship between chemical composition and conductivity is revealed in the $Li_{7-x}La_3Zr_{2-x}Ta_xO_{12}$ solid solution system. Small single-crystal samples were synthesized by a flux method so as to demonstrate the structural properties of Al-doped $Li_7La_3Zr_2O_{12}$. We also grew large single-crystal samples of $Li_{6.5}La_3Zr_{1.5}Ta_{0.5}O_{12}$ by floating zone melting method and determined the precise crystal structure using single-crystal neutron diffraction data. The lithium ion conductive properties were investigated by electrochemical measurement and NMR spectroscopy using single-crystal specimens. Novel low-temperature synthetic techniques so as to produce tetragonal $Li_7La_3Zr_2O_{12}$ and cubic $Li_{6.5}La_3Zr_{1.5}Ta_{0.5}O_{12}$ fine powders were developed.

Keywords Garnet · Crystal structure · Crystal growth · Flux method · Floating zone melting method

1 Introduction

All-solid-state Li-ion batteries (LIB) using solid electrolyte attract attention as next-generation batteries without flammable organic liquid electrolytes since the Li-ion batteries require improved safety and high energy density [1–3]. Because the characteristics of the solid electrolyte largely dominate the battery performance, many researchers have performed efforts to explore the excellent lithium ion conductors for the development of all-solid-state batteries. The solid electrolyte for all-solid-state LIB requires high lithium ion conductivity, high density, chemical stability, and electrochemical wide potential windows. Among the various kinds of solid electrolytes, oxide-based solid electrolytes show high chemical stability. Thus, a variety of oxide-based solid electrolytes showing good lithium ion conductivity

J. Akimoto (✉) · N. Hamao · K. Kataoka
National Institute of Advanced Industrial Science and Technology (AIST), Tsukuba, Japan
e-mail: j.akimoto@aist.go.jp

K. Kanamura (ed.), *Next Generation Batteries*,
https://doi.org/10.1007/978-981-33-6668-8_19

have been investigated, including the NASICON-type $Li_{1+x}Al_xTi_{2-x}(PO_4)_3$ [4], LISICON-type $Li_{2+2x}Zn_{1-x}GeO_4$ [5], perovskite-type $La_{2/3-x}Li_{3x}TiO_3$ [6], garnet-type $Li_7La_3Zr_2O_{12}$ [7], and glassy solid electrolyte materials such as in the Li_3BO_3-Li_4SiO_4 system. Among them, the garnet-type $Li_7La_3Zr_2O_{12}$ and its chemical derivatives are one of the most promising candidates because of its excellent comprehensively electrochemical performance including the electrochemical stability against lithium metal [7]. In addition, the bulk lithium ion conductivity of the Ga-doped $Li_7La_3Zr_2O_{12}$ was reported to be ~10^{-3} S cm^{-1} at room temperature, the value of which is highest among the oxide-based materials [8].

In this chapter, we review the crystal structural properties of two kinds of cubic forms and tetragonal form for $Li_7La_3Zr_2O_{12}$ from a viewpoint of lithium ion arrangement. In addition, a relationship between the crystal structure and electrochemical properties in the solid solution system $Li_{7-x}La_3Zr_{2-x}Ta_xO_{12}$ by using polycrystalline samples prepared by solid-state reaction is discussed. The conductive properties for the three kinds of $Li_{6.5}La_3M_{1.5}Ta_{0.5}O_{12}$ (M: Zr, Hf, Sn) are demonstrated. Small single-crystal samples were synthesized by a flux method so as to demonstrate the structural properties of Al-doped $Li_7La_3Zr_2O_{12}$. In addition, large single-crystal samples of $Li_{6.5}La_3Zr_{1.5}Ta_{0.5}O_{12}$ were recently grown by the floating zone melting method, and the precise crystal structure was revealed using single-crystal neutron diffraction data. The lithium ion conductive properties were investigated by electrochemical and NMR spectroscopy using the single-crystal specimens. Finally, novel low-temperature synthetic techniques so as to produce the $Li_7La_3Zr_2O_{12}$ and $Li_{6.5}La_3Zr_{1.5}Ta_{0.5}O_{12}$ fine powders are reviewed.

2 Crystal Structure of Garnet-Type Lithium Ion Conducting Oxides

The crystal structure of $Li_7La_3Zr_2O_{12}$ at room temperature belongs to the tetragonal symmetry, space group $I4_1/acd$ [9]. On the other hand, the cubic symmetry is stable only above 600 °C [10]. The high-temperature cubic garnet structure stabilizes by the substitution of Al and Ga at the Li sites, and/or by the substitution of Nb and Ta at the Zr site. Because crystal structural details such as Li–Li distance, Li–O polyhedral volume, and Li arrangement together with defect content are very important indicators to reveal the good Li-ion conduction mechanism in $Li_7La_3Zr_2O_{12}$ and its derivatives, we mention here the crystal structure of cubic Al-doped $Li_7La_3Zr_2O_{12}$ in comparison with the tetragonal structure, because the Li-ion conductivity of tetragonal $Li_7La_3Zr_2O_{12}$ is lower by two orders of magnitude than that of cubic Al-doped $Li_7La_3Zr_2O_{12}$.

In both cubic and tetragonal structures [9, 11], the garnet framework structure is composed of dodecahedral LaO_8 and octahedral ZrO_6. On the other hand, the Li atoms occupy two types of crystallographic sites in the interstices of the framework structure in the cubic phase. As shown in Fig. 1, the Li1 and Li2 atoms are located

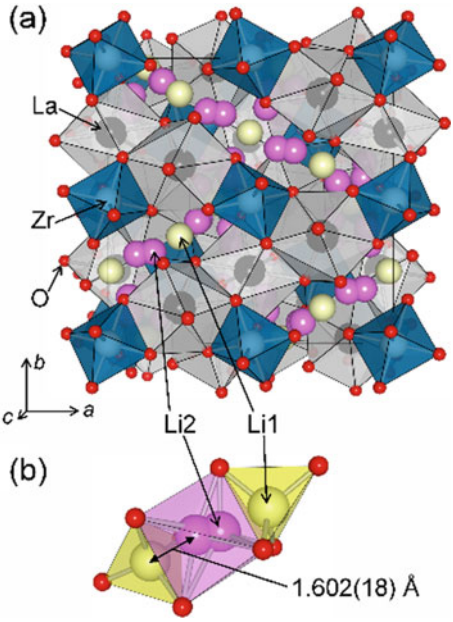

Fig. 1 **a** Crystal structure of cubic $Li_7La_3Zr_2O_{12}$. **b** Coordination polyhedra around the Li1 and Li2 sites in cubic $Li_7La_3Zr_2O_{12}$ [11]

in the tetrahedral 24*d* site and distorted octahedral 96*h* site, respectively. The Li2 site is vacant in the ideal garnet structure such as in yttrium iron garnet $Y_3Fe_5O_{12}$ (YIG). Because the Li2 atom is situated at two equivalent positions in the distorted octahedron as a positional disorder in the lithium distribution, the local coordination environment of the Li2 atom may be considered to be near fourfold LiO_4 coordination. The disordering and partial occupation of the Li atoms at the Li2 site were reported as a key role of Li-ion conduction in cubic Al-doped $Li_7La_3Zr_2O_{12}$ [11].

From a structural viewpoint, the Li-ion migration pathway should correspond to the Li atomic arrangement in the structure. As shown in Fig. 1, cubic $Li_7La_3Zr_2O_{12}$ shows the complicated Li atomic arrangement in the interstices of the garnet-type framework structure. However, by focusing attention only on the Li atoms in the structure, the basic unit of the arrangement can be simply drawn as a loop constructed by the Li1 and Li2 sites (Fig. 2). This loop links to another one, where only the Li1 site is shared by two loops as a junction, and a three-dimensional network of the Li-ion migration pathway is formed in the structure, as shown in Fig. 3.

In the loop structure, the tetrahedral $Li1O_4$ and distorted octahedral Li_2O_6 share with the face, which results in the very short Li–Li distance in this migration pathway (Fig. 1). This is a significant feature of the cubic garnet-type Li-ion conductors and may be related to the good Li-ion conductive properties compared to the other compounds.

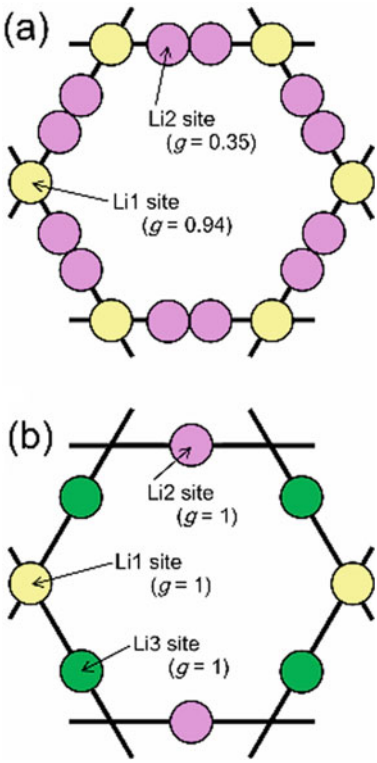

Fig. 2 The loop structures constructed by Li arrangement in **a** cubic and **b** tetragonal $Li_7La_3Zr_2O_{12}$ [11]

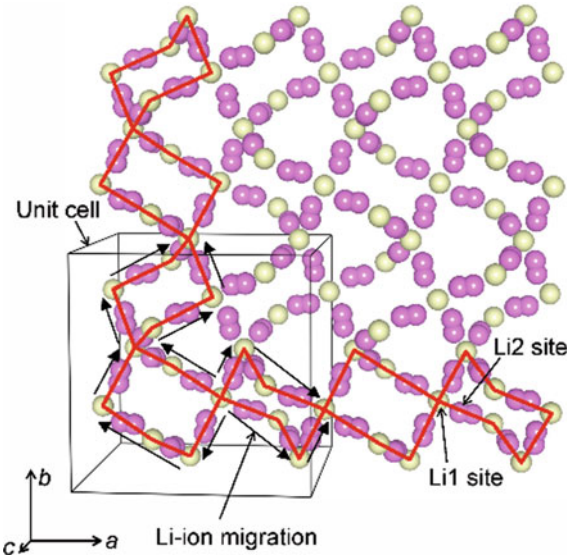

Fig. 3 Three-dimensional network structure of Li arrangement in cubic $Li_7La_3Zr_2O_{12}$ [11]

In the case of Ga-doped $Li_7La_3Zr_2O_{12}$, the Ga occupation in the loop structure causes lowering the cubic symmetry from *Ia*-3*d* to *I*-43*d* and changes the Li arrangement (Fig. 4) [8]. Unfortunately, the origin for high Li-ion conductivity in Ga-doped $Li_7La_3Zr_2O_{12}$ has not been revealed yet.

On the other hand, tetragonal $Li_7La_3Zr_2O_{12}$ shows a complete ordering of the Li atoms [9]. Namely, tetragonal $Li_7La_3Zr_2O_{12}$ has two tetrahedral sites (Li1 site and vacancy), and two distorted octahedral sites (Li2 and Li3 sites) in the loop structure (Fig. 2). The Li1, Li2, and Li3 sites are fully occupied by the Li atoms. Accordingly, the Li–Li distances over 2.5 Å are longer than those in a cubic structure.

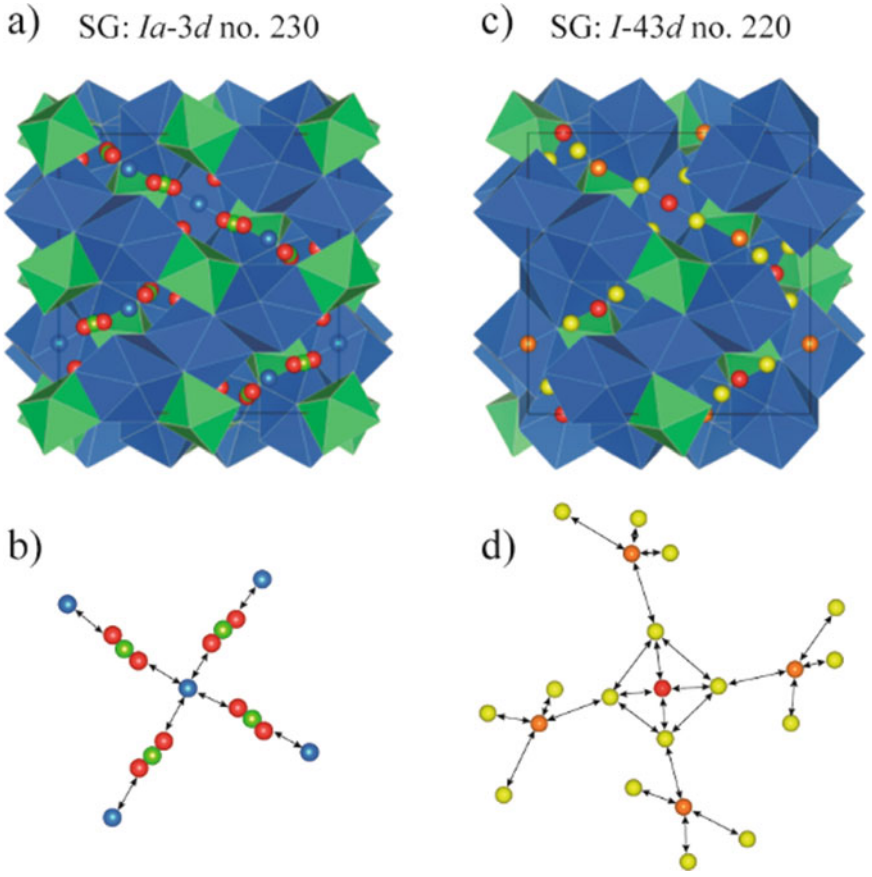

Fig. 4 **a** Crystal structure of cubic Al-doped $Li_7La_3Zr_2O_{12}$ with space group *Ia*-3*d*. The corresponding Li-ion diffusion pathway is shown in (**b**). **c** Crystal structure of cubic Ga-doped $Li_7La_3Zr_2O_{12}$ with space group *I*4-3*d*. The corresponding Li-ion diffusion pathway is shown in (**d**) [8]

3 Synthesis of Polycrystalline $Li_{7-X}La_3Zr_{2-X}Ta_xO_{12}$ by Solid-State Reaction

In order to increase the Li-ion conductivity of the garnet-type $Li_7La_3Zr_2O_{12}$, a large number of studies on the chemical substitution using various cation species have been reported. Among them, $Li_{7-x}La_3Zr_{2-x}Ta_xO_{12}$ with the cubic garnet-related-type structure shows the highest Li-ion conductivity (~ 10^{-4} S cm at 300 K) [12–14]. For this reason, the chemical and structural properties of $Li_{7-x}La_3Zr_{2-x}Ta_xO_{12}$ have been widely investigated in the literature. However, it is difficult to prepare high-quality $Li_{7-x}La_3Zr_{2-x}Ta_xO_{12}$ samples because aluminum is easily contaminated from the crucible material during the high-temperature heating. Recently, the garnet-type Al-free $Li_{7-x}La_3Zr_{2-x}Ta_xO_{12}$ samples were synthesized by some research groups [15, 16]. For example, Wang et al. reported the existence of two phases of tetragonal and cubic structures in the compositional range of $0.1 < x < 0.4$ for the Al-free $Li_{7-x}La_3Zr_{2-x}Ta_xO_{12}$ samples [16]. However, the effect of only Ta substitution on the structural property and the Li-ion conductivity has not been clarified yet.

Recently, the garnet-type Al-free $Li_{7-x}La_3Zr_{2-x}Ta_xO_{12}$ ($0 \leq x \leq 0.6$) samples were synthesized by the conventional solid-state synthesis method under Al-free conditions [17]. In addition, the influence of Ta substitution on the crystal phase formation and the Li-ion conductive properties was demonstrated [17]. The starting materials used were Li_2CO_3, La_2O_3, ZrO_2, and Ta_2O_5 in this method. An excess Li source was added to compensate for the volatilization of lithium during the high-temperature calcination. These materials were mixed by ball milling and calcined at 1127 K in air. Then, the pressed pellets were sintered at 1373 K in the air using YSZ crucibles. At the sintering step, the pellets were covered with the mother powder of the same composition to prevent the Li loss.

Figure 5 shows the lattice parameters of the $Li_{7-x}La_3Zr_{2-x}Ta_xO_{12}$ ($0 \leq x \leq 0.6$) samples. The XRD patterns for $Li_7La_3Zr_2O_{12}$ ($x = 0$) and $Li_{6.4}La_3Zr_{1.4}Ta_{0.6}O_{12}$ ($x = 0.6$) samples were assigned to be single phases of tetragonal (space group: $I4_1/acd$) and cubic (space group: $Ia\text{-}3d$) structures, respectively. On the other hand, the intermediate compositional samples of $Li_{7-x}La_3Zr_{2-x}Ta_xO_{12}$ ($0.2 \leq x \leq 0.5$) showed a coexistence of both the tetragonal and cubic phases.

All of the Al-free $Li_{7-x}La_3Zr_{2-x}Ta_xO_{12}$ ($0 \leq x \leq 0.6$) samples exhibit relatively high conductivity of ~ 10^{-4} S cm^{-1} at room temperature, and the $Li_{6.5}La_3Zr_{1.5}Ta_{0.5}O_{12}$ ($x = 0.5$) sample shows the highest Li-ion conductivity of 8.4×10^{-4} S cm^{-1} at room temperature. In order to clarify the relationship between the Li-ion conductivity and the Li-ion arrangement, the crystal structure analysis of $Li_{7-x}La_3Zr_{2-x}Ta_xO_{12}$ ($0 \leq x \leq 0.6$) was performed by Rietveld analysis using powder X-ray diffraction data. Figure 6 shows the loop structure of the Li arrangement for the $x = 0.2$ and $x = 0.5$ samples. The Li2 atom at 96*h* site is gradually shifted together with increasing Ta-content from $x = 0.2$ to 0.5, resulting in the shorter Li–Li distance in the loop structure of the cubic garnet-type framework structure. Accordingly, the optimum Li arrangement in the loop structure can be established in the $x = 0.5$ composition from a viewpoint of Li conductivity [17].

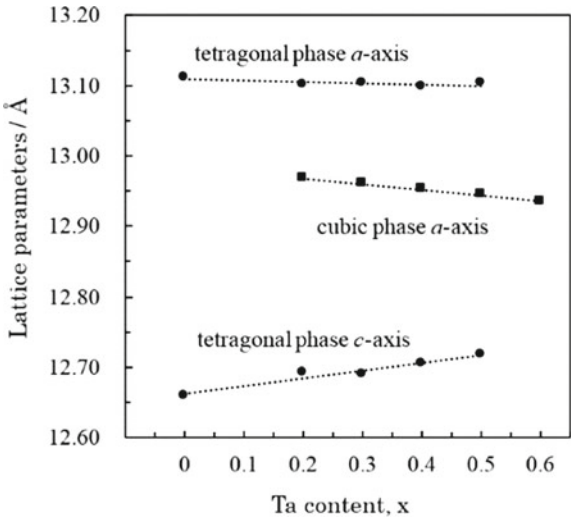

Fig. 5 Lattice parameters of the Al-free $Li_{7-x}La_3Zr_{2-x}Ta_xO_{12}$ ($0 \leq x \leq 0.6$) samples [17]

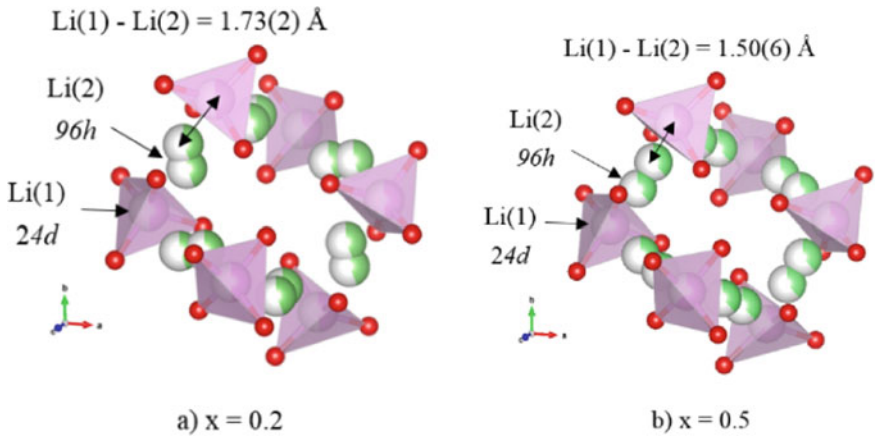

Fig. 6 The coordination polyhedral around Li sites for $Li_{7-x}La_3Zr_{2-x}Ta_xO_{12}$ with **a** $x = 0.2$ and **b** $x = 0.5$ samples [17]

4 Synthesis of Polycrystalline $Li_{6.5}La_3M_{1.5}Ta_{0.5}O_{12}$ (*M*: Zr, Hf, Sn) by Solid-State Reaction

Tantalum is one of the most effective dopants for the garnet-type oxide, and the optimum Ta-content is nearly 0.5 per unit formula, as previously demonstrated in Ref. [17]. Therefore, we focused on the Ta-content of 0.5 for garnet-type oxide having the cubic structure. It is well known that $Li_7La_3Sn_2O_{12}$ [18] and $Li_7La_3Hf_2O_{12}$ [19]

also belong to the tetragonal structure such as $Li_7La_3Zr_2O_{12}$. However, the optimized dopant for $Li_7La_3Sn_2O_{12}$ and $Li_7La_3Hf_2O_{12}$ have not been examined yet including the amount of substitution. It can be expected that the Li-ion conductivity of $Li_7La_3Sn_2O_{12}$ and $Li_7La_3Hf_2O_{12}$ is also improved by Ta substitution for Sn and/or Hf site. Furthermore, the chemical stability of garnet-related-type $Li_7La_3M_2O_{12}$ (*M*: Zr, Hf, Sn) to carbonate and hydroxide was recently reported by first-principle calculation using DFT calculation [20]. Kang et al. reported that $Li_7La_3Sn_2O_{12}$ showed higher chemical stability than the other two materials [20]. Therefore, $Li_7La_3Sn_2O_{12}$ could be expected for solid electrolyte as all-solid-state Li-ion batteries. However, Li-ion conductive properties and crystal structure parameters of $Li_7La_3Sn_2O_{12}$ which has a cubic system by cation substitution have not been clarified yet.

Recently, the garnet-type oxide $Li_{6.5}La_3Hf_{1.5}Ta_{0.5}O_{12}$ and $Li_{6.5}La_3Sn_{1.5}Ta_{0.5}O_{12}$ samples were prepared by conventional solid-state reaction method using HfO_2 and SnO_2 as starting materials according to the reported procedure as previously described in Ref. [21]. Figure 7 shows the powder X-ray diffraction patterns of $Li_{6.5}La_3Hf_{1.5}Ta_{0.5}O_{12}$ and $Li_{6.5}La_3Sn_{1.5}Ta_{0.5}O_{12}$. All diffraction peaks can be attributed to a single phase of cubic garnet-type structure having the space group of *Ia*-3*d*. Figure 8 shows the cross-sectional morphology of $Li_{6.5}La_3Hf_{1.5}Ta_{0.5}O_{12}$ and $Li_{6.5}La_3Sn_{1.5}Ta_{0.5}O_{12}$ after sintering at 1150 °C. These samples have a high relative density above 90%. The small and homogeneous grain size distributions are observed in the $Li_{6.5}La_3Hf_{1.5}Ta_{0.5}O_{12}$ sample. All of the Ta substituted samples exhibit a relatively high conductivity of ~10^{-4} S cm^{-1} at room temperature, and the activation energies of $Li_{6.5}La_3Hf_{1.5}Ta_{0.5}O_{12}$ and $Li_{6.5}La_3Sn_{1.5}Ta_{0.5}O_{12}$, which were determined from the Arrhenius plots, are $E_a = 0.40$ and 0.45 eV, respectively (Fig. 9). The value of $Li_{6.5}La_3Hf_{1.5}Ta_{0.5}O_{12}$ is smaller than that (0.43 eV) of $Li_{6.5}La_3Zr_{1.5}Ta_{0.5}O_{12}$.

The crystal structure was analyzed by the Rietveld method using powder X-ray diffraction data [21]. The unit cell volumes and octahedral (*M*, Ta)O_6 volumes for $Li_{6.5}La_3M_{1.5}Ta_{0.5}O_{12}$ (*M*: Zr, Hf, Sn) decrease together with decreasing ionic radii

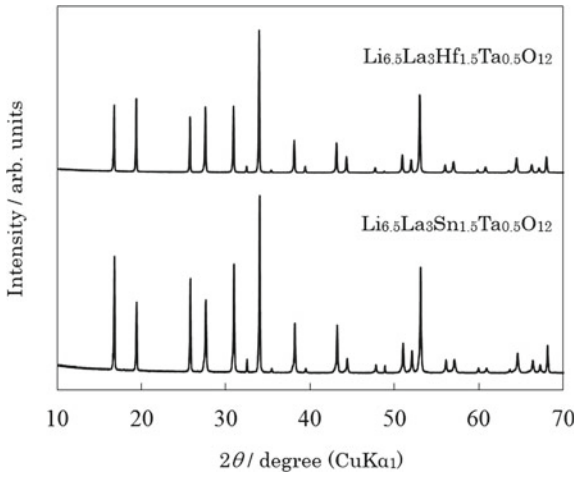

Fig. 7 Powder X-ray diffraction patterns of $Li_{6.5}La_3Hf_{1.5}Ta_{0.5}O_{12}$ and $Li_{6.5}La_3Sn_{1.5}Ta_{0.5}O_{12}$ [21]

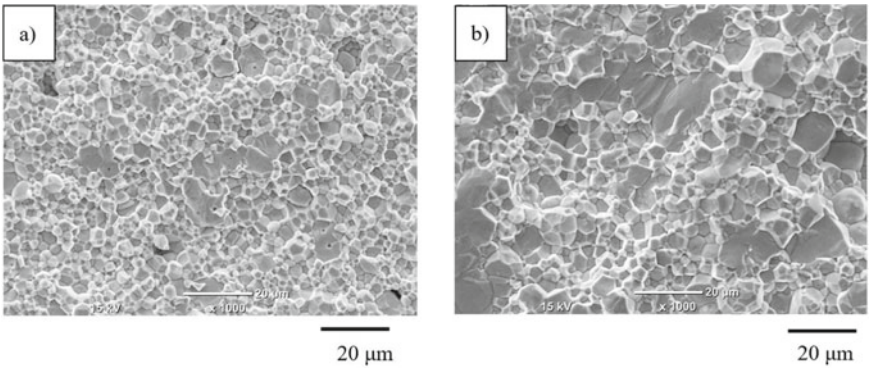

Fig. 8 SEM images of the cross-sectional morphology of **a** $Li_{6.5}La_3Hf_{1.5}Ta_{0.5}O_{12}$ and **b** $Li_{6.5}La_3Sn_{1.5}Ta_{0.5}O_{12}$ [21]

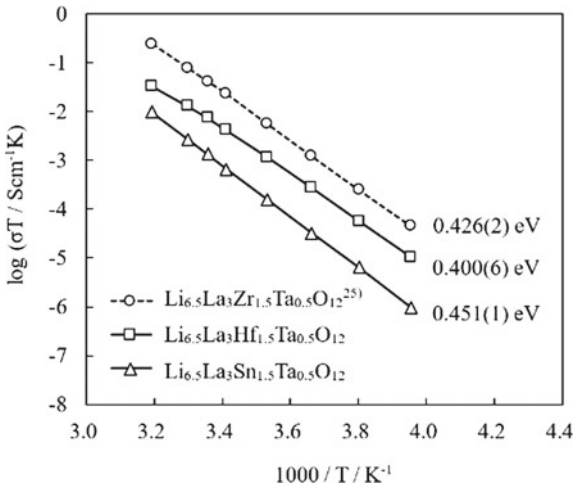

Fig. 9 Arrhenius plots of total conductivities of $Li_{6.5}La_3M_{1.5}Ta_{0.5}O_{12}$ (*M*: Zr, Hf, Sn) [21]

of M^{4+} cations (0.72 Å for Zr^{4+}, 0.71 Å for Hf $^{4+}$, and 0.69 Å for Sn^{4+}). However, the polyhedral volumes of $Li1O_4$ and Li_2O_6 in $Li_{6.5}La_3Hf_{1.5}Ta_{0.5}O_{12}$ are the largest among these $Li_{6.5}La_3M_{1.5}Ta_{0.5}O_{12}$ compounds. It has been suggested that the bottleneck for Li-ion diffusion from Li 24*d* site to Li 96*h* site is the face of shared edges of neighboring Li site in the garnet-type structure. Therefore, Li-ion conductivity is affected by the polyhedral volume of $Li1O_4$. Since $Li_{6.5}La_3Hf_{1.5}Ta_{0.5}O_{12}$ has a larger polyhedral volume of $Li1O_4$ and $Li2O_6$ in the crystal structure, the Li-ion conductive space is wider than $Li_{6.5}La_3Hf_{1.5}Ta_{0.5}O_{12}$, which diffuse from tetrahedral site to octahedral site. This fact may suggest the lowest activation energy observed in the $Li_{6.5}La_3Hf_{1.5}Ta_{0.5}O_{12}$ sample. From a viewpoint of the Li–O polyhedral volume in the unit cell, it is concluded that $Li_{6.5}La_3Hf_{1.5}Ta_{0.5}O_{12}$ has a most suitable Li-ion

environment among the $Li_{6.5}La_3M_{1.5}Ta_{0.5}O_{12}$ (M: Zr, Hf, Sn) compounds from a viewpoint of Li conductivity [21].

5 Low-Temperature Synthesis of Tetragonal $Li_7La_3Zr_2O_{12}$ by Co-Precipitation Method

The particle size and morphology are important for the production of a thin film and sintering body for solid electrolyte in all-solid-state battery. For this reason, low-temperature synthetic techniques such as the sol-gel method and the co-precipitation method have been applied so as to produce fine particle samples for garnet-type materials [22–25]. In fact, the uniform and small particle sample of the garnet-type materials was reported by several low-temperature synthetic techniques. For example, Kokal et al. reported the synthesis of tetragonal $Li_7La_3Zr_2O_{12}$ powder prepared by the modified Pechini sol-gel method [22]. The grain size of their powder sample was reported to be ranged from 500 nm to 2 μm.

A similar feature was recently reported in garnet-related-type $Li_{6.75}La_3Zr_{1.75}Nb_{0.25}O_{12}$ prepared by the co-precipitation method [26]. The primary particle size prepared by the co-precipitation method was reported to be 50–100 nm for the $Li_{6.75}La_3Zr_{1.75}Nb_{0.25}O_{12}$ sample, which was much smaller than that by the solid-state synthetic method. Therefore, it is considered that the control of the particle morphology for the garnet materials was affected by the particle size of the precursor.

Recently, we synthesized a tetragonal garnet-type $Li_7La_3Zr_2O_{12}$ sample by the co-precipitation method using LiOH solution, in order to control the particle size and morphology of the $Li_7La_3Zr_2O_{12}$ powder for the first time [27]. Stoichiometric amounts of $LaCl_3 \cdot 7H_2O$ and $ZrOCl_2 \cdot 8H_2O$ were dissolved in distilled water. Then, the LiOH solution was added slowly into the mixed solution prepared above until the solution pH became 8–9. The precipitated precursor, which was composed of lanthanum hydroxide and zirconium hydroxide, was evaporated and washed with distilled water and was dried at 80 °C overnight. Next, in order to obtain the $Li_7La_3Zr_2O_{12}$ sample, stoichiometric $LiOH \cdot H_2O$ was added into the ground precursor. Finally, the mixture was calcined at 950 °C for 10 h in the air using an alumina crucible. The particle morphology of the obtained $Li_7La_3Zr_2O_{12}$ sample was elliptical in shape and the primary grain size was smaller than the conventional solid-state method, as shown in Fig. 10. The result of the particle size distribution measurement shows that the average secondary particle size was approximately 9.66 μm, even after calcination at 950 °C with a relatively narrow distribution [27].

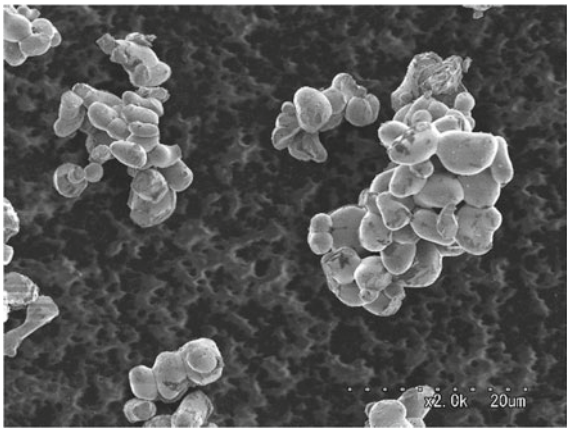

Fig. 10 FE-SEM images of the particle morphology of $Li_7La_3Zr_2O_{12}$ prepared by co-precipitation method [27]

6 Low-Temperature Synthesis of $Li_{6.5}La_3Zr_{1.5}Ta_{0.5}O_{12}$ Using Precursor Oxides

The garnet-type $Li_{6.5}La_3Zr_{1.5}Ta_{0.5}O_{12}$ samples having high Li-ion conductivity have been synthesized by conventional solid-state reaction. However, a high temperature above 1100 °C is needed to prepare a single-phase $Li_{6.5}La_3Zr_{1.5}Ta_{0.5}O_{12}$ sample by this synthetic method. From a viewpoint of the interface between solid electrolyte and electrode materials in all-solid-state battery, lowering the synthetic temperature is important so as to avoid the reaction between these materials at the interface. In the case of $Li_7La_3Zr_2O_{12}$, various low-temperature synthetic methods using sol-gel and/or co-precipitation processes [22–25] or some precursor materials such as pyrochlore-type $La_2Zr_2O_7$ [28, 29] have been developed to avoid Li loss during high-temperature treatment. However, $Li_{6.5}La_3Zr_{1.5}Ta_{0.5}O_{12}$ samples have not been synthesized yet by such low-temperature methods.

Recently, we successfully synthesized a garnet-type $Li_{6.5}La_3Zr_{1.5}Ta_{0.5}O_{12}$ polycrystalline sample at a relatively low temperature of 700 °C using pyrochlore-type $La_2Zr_2O_7$ and weberite-type La_3TaO_7 as precursor oxides [30]. In this synthetic procedure, the precursor materials of pyrochlore-type $La_2Zr_2O_7$ and weberite-type La_3TaO_7 were first synthesized via conventional solid-state reactions using La_2O_3, ZrO_2, and Ta_2O_5 as starting materials. Stoichiometric amounts of these oxides were ball-milled using zirconia balls in ethanol for 2 h. Then, the obtained mixtures were calcined between 1200 and 1300 °C for 12 h in the air using an intermediate grinding. Next, the stoichiometric amount of $LiOH{\cdot}H_2O$ and the obtained precursor materials were mixed according to the following Eq. (1):

$$6.5\,LiOH \cdot H_2O + 0.75\,La_2Zr_2O_7 + 0.5\,La_3TaO_7 \rightarrow Li_{6.5}La_3Zr_{1.5}Ta_{0.5}O_{12} + 9.75\,H_2O \quad (1)$$

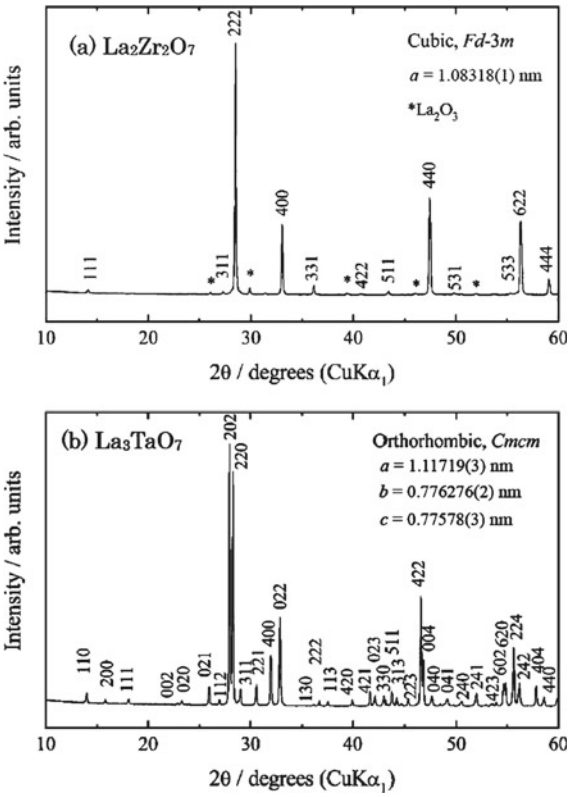

Fig. 11 Powder XRD patterns of **a** pyrochlore-type $La_2Zr_2O_7$ and **b** weberite-type La_3TaO_7 samples [31]

Then, the mixture was calcined at 700 °C for 12 h in the air using a high-purity alumina crucible.

Figure 11 shows the XRD patterns of pyrochlore-type $La_2Zr_2O_7$ and weberite-type La_3TaO_7 as precursor oxides, respectively. The main peaks of both the samples are well-indexed to the structural data of cubic pyrochlore-type $La_2Zr_2O_7$ (space group: *Fd*-3*m*) [31] and orthorhombic weberite-type La_3TaO_7 (space group: *Cmcm*) [32], respectively. Figure 12 shows the XRD pattern of the garnet-type $Li_{6.5}La_3Zr_{1.5}Ta_{0.5}O_{12}$ prepared using the present precursor oxides. All of the observed peaks can be indexed to the cubic garnet-type structure (space group: *Ia*-3*d*), and no impurity phase was observed. The lattice parameter was determined to be $a = 12.9577(1)$ Å by the least-squares method. Accordingly, the garnet-type $Li_{6.5}La_3Zr_{1.5}Ta_{0.5}O_{12}$ was successfully synthesized using $La_2Zr_2O_7$ and La_3TaO_7 as precursor materials at a relatively low temperature of 700 °C. The primary particle size of the present $Li_{6.5}La_3Zr_{1.5}Ta_{0.5}O_{12}$ sample was about 2 μm, as shown in Fig. 13, which is considerably smaller than that prepared by conventional solid-state reaction at higher temperatures. Thermo-gravimetry differential thermal analysis data confirmed that the reaction between $LiOH{\cdot}H_2O$ and precursor oxides occurred above 500 °C after the dehydration reaction of $LiOH{\cdot}H_2O$ [30].

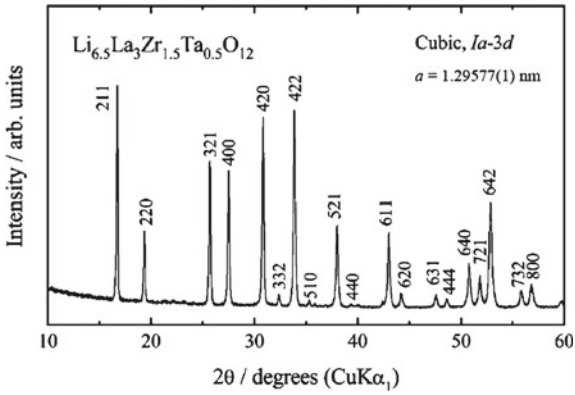

Fig. 12 Powder XRD pattern of garnet-type $Li_{6.5}La_3Zr_{1.5}Ta_{0.5}O_{12}$ sample prepared using the precursor oxides [31]

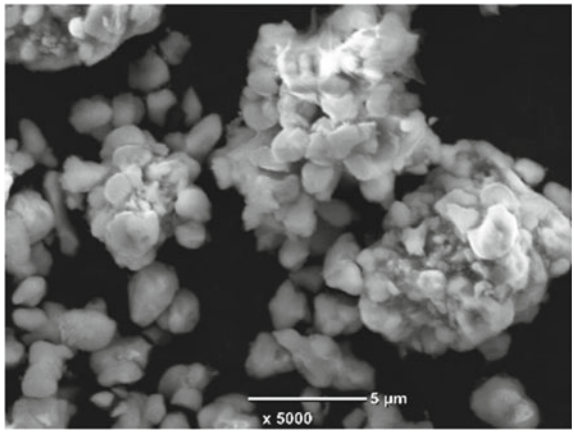

Fig. 13 SEM image of garnet-type $Li_{6.5}La_3Zr_{1.5}Ta_{0.5}O_{12}$ sample prepared using the precursor oxides [31]

7 Synthesis of al-Doped $Li_7La_3Zr_2O_{12}$ Single Crystals by a Flux Method

Single-crystal specimens have highly been desired to clarify the physical and electrochemical properties. Especially, the intrinsic bulk and/or anisotropic conductive properties can be measured using the single-crystal specimens, as we have previously demonstrated in electrical conductivity measurements using $LiCoO_2$ and Li_xCoO_2 single crystals [33–35] and in electrochemical measurements of the chemical diffusion coefficients of Li-ion in the spinel-type $LiMn_2O_4$ [36, 37]. The single-crystal samples of such lithium transition oxides have been synthesized by a flux method at relatively lower temperatures, because of the high volatility of lithium oxide components at high temperatures.

Single-crystal samples of garnet-type $Li_7La_3Zr_2O_{12}$ with the garnet-type structure were successfully synthesized by a self-flux method using some lithium salts at high temperatures [9, 11, 38]. The tetragonal form of $Li_7La_3Zr_2O_{12}$ crystals was prepared

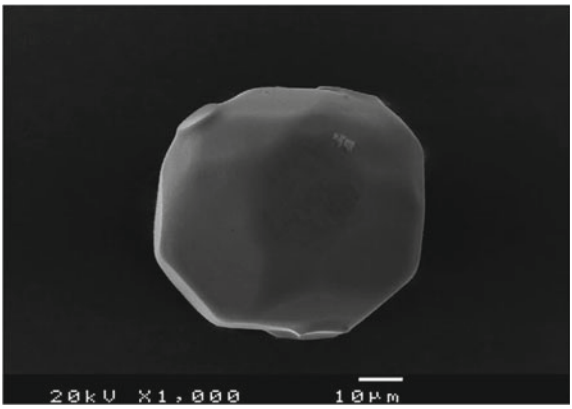

Fig. 14 SEM micrograph of a single crystal of tetragonal $Li_7La_3Zr_2O_{12}$ [9]

using Li_2CO_3 as a flux material at 1313 K in a gold crucible [9]. The crystals were separated from the solidified melts by immersing the gold crucible in hot water. Figure 14 shows the typical photograph of tetragonal $Li_7La_3Zr_2O_{12}$ crystals. The grown crystals are colorless and transparent; they also had a spherical shape with a maximum diameter of 0.05 mm in size.

The cubic $Li_7La_3Zr_2O_{12}$ was first synthesized by high-temperature heating at 1250 °C, and its crystal structure was determined using single-crystal X-ray diffraction data [11]. However, the obtained crystal size was 0.05 mm in diameter which was too small to evaluate the physical properties of the cubic $Li_7La_3Zr_2O_{12}$.

Single crystals of cubic Al-doped $Li_7La_3Zr_2O_{12}$ having larger size were synthesized by a self-flux method using $LiNO_3$ as a starting component at 1150 °C [38]. The starting materials of La_2O_3 and ZrO_2 were first well-mixed in a nominal molar ratio of La: Zr = 3: 2. These were further mixed by excess $LiNO_3$ as self-flux material. The powder mixture was charged into a high-purity alumina crucible, and the temperature was elevated to 1150 °C in air, and then held for 4 h. The obtained crystals were separated from the solidified flux materials by immersing the alumina crucible in hot water.

Figure 15 shows the obtained single crystals of Al-doped $Li_7La_3Zr_2O_{12}$ grown at 1150 °C using $LiNO_3$ as a self-flux material in a starting molar ratio of Li: La: Zr = 20: 3: 2. The crystals were colorless and transparent and had a polyhedral shape with a maximum dimension of 0.15 × 0.10 × 0.10 mm^3. The well-formed crystal morphology with facets can be observed in the SEM photograph [38].

The lattice parameter was determined by the powder XRD data of the pulverized single crystals to be $a = 13.00(3)$ Å. This value was slightly larger than those in the previous reports for Al-doped $Li_7La_3Zr_2O_{12}$ [7, 11]. This fact may suggest that the Li^+/H^+ ion exchange reaction has proceeded in the washing procedure using hot water. We should treat carefully the grown crystals from the solidified flux material in the case of the flux method.

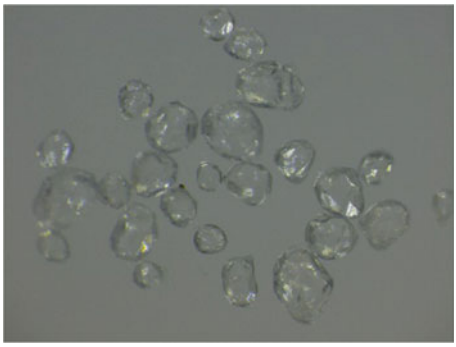

Fig. 15 Single crystals of cubic $Li_7La_3Zr_2O_{12}$ grown at 1150 °C using $LiNO_3$ as a self-flux material

8 Crystal Growth of $Li_{6.5}La_3Zr_{1.5}Ta_{0.5}O_{12}$ Single Crystals by Melt Growth Technique

The centimeter-sized large single crystals of garnet-type oxide materials were recently synthesized from the high-temperature melt. The melt growth technique is usually used for the industrial single-crystal growth such as semiconducting Si, $LiNbO_3$, and $LiTaO_3$. The first report for the lithium ion conducting garnet-type oxides from the melt was single-crystal growth of $Li_5La_3Ta_2O_{12}$ [39], while the experimental details for crystal growth were not reported. Recently, single crystals of $Li_6La_3ZrTaO_{12}$ were grown by the Czochralski (Cz) method, and NMR measurement using a single-crystal sample was reported [40]. Furthermore, single crystals of $Li_{7-x}La_3Zr_{2-x}Nb_xO_{12}$ and $Li_{7-x}La_3Zr_{2-x}Ta_xO_{12}$ were grown by using the floating zone (FZ) melting method [41–43]. From these reports, melt growth techniques such as Cz and FZ method are thought to be useful and suitable for crystal growth of the garnet-type lithium ion conducting oxides.

In the case of FZ method, the sample preparation was reported to be carried out in two steps [42]. The first step is the preparation of the raw materials by a conventional solid-state reaction. A mixture of Li_2CO_3, La_2O_3, ZrO_2, and Ta_2O_5 was heated at 1123 K in the air. In this case, 20% excess composition for the lithium-content was employed so as to prevent the compositional deviation due to the volatilization of lithium during the crystal growth. The sample was reground and isostatically pressed to form a cylindrical shape. The formed rods were subsequently sintered at 1423 K for 4 h in air. The second step is the crystal growth using an optical image furnace equipped with four halogen lamps.

Centimeter-sized single-crystal rods of $Li_{6.5}La_3Zr_{1.5}Ta_{0.5}O_{12}$ were grown by floating zone melting technique [42, 43]. The typical size of the single-crystal rod was 8 mm in diameter and 70 mm in length, as shown in Fig. 16. $Li_{6.5}La_3Zr_{1.5}Ta_{0.5}O_{12}$ crystallizes in a cubic structure with an *Ia*-3*d* space group and the lattice parameter $a = 12.9455\ (6)$ Å [42]. From the results of structure refinement using single-crystal neutron diffraction data [42], occupation sites for lithium atoms were determined to be two crystallographic sites: the distorted tetrahedral 96*h* site and the distorted

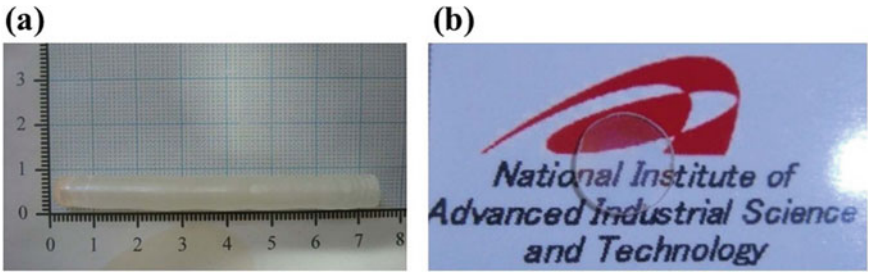

Fig. 16 **a** As-grown $Li_{6.5}La_3Zr_{1.5}Ta_{0.5}O_{12}$ single-crystal rod and **b** a polished $Li_{6.5}La_3Zr_{1.5}Ta_{0.5}O_{12}$ single-crystal plate [42]

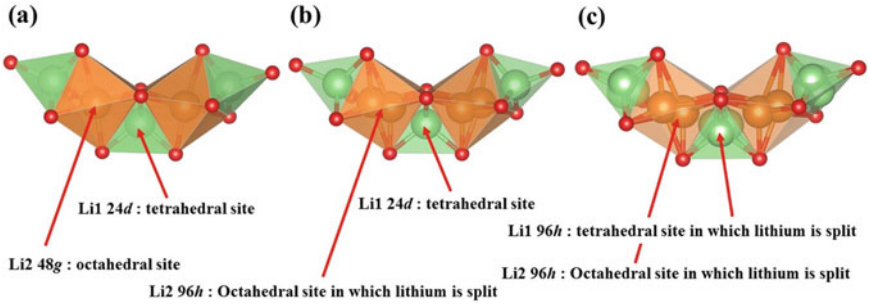

Fig. 17 Three kinds of Li arrangement models; **a** completely ordering model in tetragonal $Li_7La_3Zr_2O_{12}$, **b** partly disordering model as previously reported, and **c** completely disordering model in $Li_{6.5}La_3Zr_{1.5}Ta_{0.5}O_{12}$ determined using single-crystal neutron diffraction data [42]

octahedral 96*h* site (Fig. 17). The total Li-ion conductivity of $Li_{6.5}La_3Zr_{1.5}Ta_{0.5}O_{12}$ was determined to be 1.27×10^{-3} S cm^{-1} at 298 K by AC impedance measurements (Fig. 18). This value is the highest among the reported garnet-type materials, and it is concluded that the bulk nature of conductivity can be utilized as total conductivity in the case of the single-crystal solid electrolyte because there is no grain boundary in the single-crystal solid. Using NMR spectroscopy [42, 44–46], we determined the Li diffusion coefficient to be 1.57×10^{13} m^2 s^{-1} at 298 K and 7.96×10^{13} m^2 s^{-1} at 333 K [42]. These values related to Li-ion migration are higher than those reported for polycrystalline samples.

9 Concluding Remarks

In this chapter, the recent advancements of the garnet-type lithium ion conducting oxide materials including not only large-sized single-crystal growth but also small particle synthesized at lower temperatures has been reviewed. The intrinsic bulk nature of the conductive properties and the precise structural properties have been

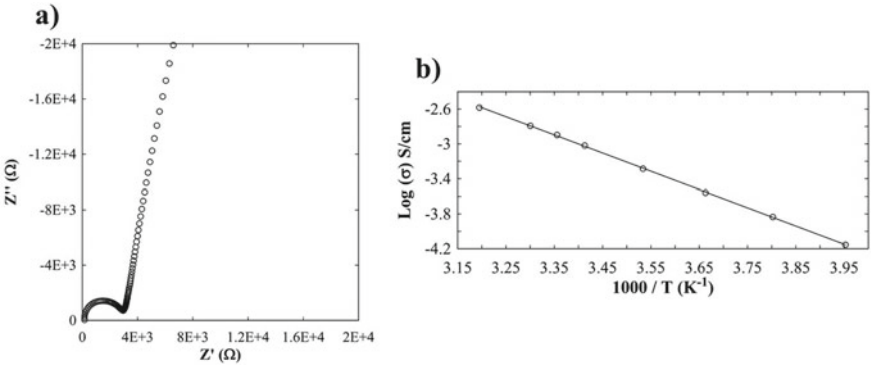

Fig. 18 **a** AC impedance Nyquist plot of the $Li_{6.5}La_3Zr_{1.5}Ta_{0.5}O_{12}$ single-crystal plate at 298 K. **b** Temperature dependence of the Li-ion conductivity for the $Li_{6.5}La_3Zr_{1.5}Ta_{0.5}O_{12}$ single-crystal plate [42]

revealed using the single-crystal samples for the first time. We believe the advantage of single-crystal solid electrolyte for the battery application from viewpoints of low resistance of separator and high critical current density against the lithium penetration phenomena. We are now trying to improve the lithium ion conductivity of the garnet materials by additional chemical modifications and optimization of the local Li arrangement in the loop structure constructing by the garnet-type framework structure.

Acknowledgements The authors thank Dr. Hiroshi Nagata and Dr. Norihito Kijima of AIST for the electrochemical measurements and valuable discussions. A part of this study was financially supported by the Advanced Low Carbon Technology Research and Development Program (ALCA-SPRING) from Japan Science and Technology Agency (JST).

References

1. Goodenough, J. B., & Kim, Y. (2010). *Chemistry of Materials, 22,* 587–603.
2. Armand, M., & Tarascon, J. M. (2008). *Nature, 451,* 652–657.
3. Janek, J., & Zeier, W. G. (2016). *Nature Energy, 1,* 16041.
4. Hong, H. Y. –P. (1978). *Materials Research Bulletin, 13,* 117–124.
5. Aono, H., Sugimoto, E., Sadaoka, Y., Imanaka, N., & Adachi, G. (1989). *Journal of the Electrochemical Society, 136,* 590–591.
6. Inaguma, Y., Liquan, C., Itoh, M., Nakamura, T., Uchida, T., Ikuta, H., et al. (1993). *Solid State Communications, 86,* 689–693.
7. Murugan, R., Thangadurai, V., & Weppner, W. (2007). *Angewandte Chemie International Edition, 46,* 7778–7781.
8. Rettenwander, D., Redhammer, G., Preishuber-Pflügl, F., Cheng, L., Miara, L., Wagner, R., et al. (2016). *Chemistry of Materials, 28,* 2384–2392.
9. Awaka, J., Kijima, N., Hayakawa, H., & Akimoto, J. (2009). *Journal of Solid State Chemistry, 182,* 2046–2052.

10. Matsui, M., Takahashi, K., Sakamoto, K., Hirano, A., Takeda, Y., Yamamoto, O., et al. (2014). *Dalton Transactions, 43,* 1019–1024.
11. Awaka, J., Takashima, A., Kataoka, K., Kijima, N., Idemoto, Y., & Akimoto, J. (2011). *Chemistry Letters, 40,* 60–62.
12. Li, Y., Wang, C., Xie, H., Cheng, J., & Goodenough, J. B. (2011). *Electrochemistry Communications, 13,* 1289–1292.
13. Allen, J. L., Wolfenstine, J., Rangasamy, E., & Sakamoto, J. (2012). *Journal of Power Sources, 206,* 315–319.
14. Buschmann, H., Berendts, S., Mogwitz, B., & Janek, J. (2012). *Journal of Power Sources, 206,* 236–244.
15. Thompson, T., Wolfenstine, J., Allen, J. L., Johannes, M., Huq, A., David, I. N., et al. (2014). *Journal of Materials Chemistry A, 2,* 13431–13436.
16. Wang, Y., & Lai, W. (2015). *Journal of Power Sources, 275,* 612–620.
17. Hamao, N., Kataoka, K., Kijima, N., & Akimoto, J. (2016). *Journal of the Ceramic Society of Japan, 124,* 678–683.
18. Percival, J., Kendrick, E., Smith, R. I., & Slater, P. R. (2009). *Dalton Transactions, 26,* 5177–5181.
19. Awaka, J., Kijima, N., Kataoka, K., Hayakawa, H., Ohshima, K., & Akimoto, J. (2010). *Journal of Solid State Chemistry, 183,* 180–185.
20. Kang, S. G., & Sholl, D. S. (2014). *Journal of Physical Chemistry C, 118,* 17402–17406.
21. Hamao, N., Kataoka, K., & Akimoto, J. (2017). *Journal of the Ceramic Society of Japan, 125,* 272–275.
22. Kokal, I., Somer, M., Notten, P. H. L., & Hintzen, H. T. (2011). *Solid State Ionics, 185,* 42–46.
23. Janani, N., Ramakumar, S., Dhivya, L., Deviannapoorani, C., Saranya, K., Murugan, R. (2011). *Ionics*, *17,* 575–580.
24. Toda, S., Ishiguro, K., Shimonishi, A., Hirano, A., Takeda, Y., Yamamoto, O., et al. (2013). *Solid State Ionics, 233,* 102–106.
25. Takano, R., Tadanaga, K., Hayashi, A., & Tatsumisago, N. (2014). *Solid State Ionics, 255,* 104–107.
26. Imagawa, H., Ohta, S., Kihira, Y., & Asaoka, T. (2014). *Solid State Ionics, 262,* 609–612.
27. Hamao, N., & Akimoto, J. (2015). *Chemistry Letters, 44,* 970–972.
28. Deviannapoorani, C., Ramakumar, S., Janani, N., & Murugan, R. (2015). *Solid State Ionics, 283,* 123–130.
29. Kimura, T., Yamada, Y., Yamamoto, K., Matsuda, T., Nomura, H., & Hirayama, T. (2017). *Journal of the American Ceramic Society, 100,* 1313–1319.
30. Hamao, N., & Akimoto, J. (2019). *Journal of the Ceramic Society of Japan, 127,* 374–477.
31. Tabira, Y., Withers, R. L., Yamada, T., & Ishizawa, N. (2001). *Zeitschrift für Kristallographie, 216,* 92–98.
32. Wakeshima, M., Nishimine, H., & Hinatsu, Y. (2004). *Journal of Physics: Condensed Matter, 16,* 4103–4120.
33. Akimoto, J., Gotoh, Y., & Oosawa, Y. (1998). *Journal of Solid State Chemistry, 141,* 298–302.
34. Takahashi, Y., Gotoh, Y., Akimoto, J., Mizuta, S., Tokiwa, K., & Watanabe, T. (2002). *Journal of Solid State Chemistry, 164,* 1–4.
35. Takahashi, Y., Kijima, N., Dokko, K., Nishizawa, M., Uchida, I., & Akimoto, J. (2007). *Journal of Solid State Chemistry, 180,* 313–321.
36. Akimoto, J., Takahashi, Y., Gotoh, Y., & Mizuta, S. (2000). *Chemistry of Materials, 12,* 3246–3248.
37. Dokko, K., Nishizawa, M., Mohamedi, M., Umeda, M., Uchida, I., Akimoto, J., et al. (2001). *Electrochemical and Solid-State Letters, 4,* A151–A153.
38. Awaka, J., Takashima, A., Hayakawa, H., Kijima, N., Idemoto, Y., & Akimoto, J. (2011). *Key Engineering Materials, 485,* 99–102.
39. Hyooma, H., & Hayashi, K. (1988). *Materials Research Bulletin, 23,* 1399–1407.
40. Stanje, B., Rettenwander, D., Breuer, S., Uitz, M., Berendts, S., Lerch, M., et al. (2017). *Annalen der Physik, 529,* 1700140.

41. Kataoka, K., Nagata, H., & Akimoto, J. (2018). *Scientific Reports, 8,* 9965.
42. Kataoka, K., & Akimoto, J. (2018). *ChemElectroChem, 5,* 2551–2557.
43. Kataoka, K., & Akimoto, J. (2019). *Journal of the Ceramic Society of Japan, 127,* 521–526.
44. Dorai, A., Kuwata, N., Takekawa, R., Kawamura, J., Kataoka, K., & Akimoto, J. (2018). *Solid State Ionics, 327,* 18–26.
45. Hayamizu, K., Terada, Y., Kataoka, K., & Akimoto, J. (2019). *The Journal of Chemical Physics—AIP Publishing—Scitation, 150,* 194502.
46. Hayamizu, K., Terada, Y., Kataoka, K., Akimoto, J., & Haishi, T. (2019). *Physical Chemistry Chemical Physics: PCCP, 21,* 23589–23597.